CONFERENCE PRE-PRINT

INTERPRETING STRUCTURES OBSERVED IN PELLET ABLATION PROFILES IN THE STELLARATOR TJ-II

K. J. McCARTHY Laboratorio Nacional de Fusión, CIEMAT Madrid, Spain Email: kieran.mccarthy@ciemat.es

I. GARCÍA-CORTÉS, B. van MILLIGEN, A. BACIERO, R. CARRASCO, T. ESTRADA, R. GARCÍA, J. HERNÁNDEZ SÁNCHEZ, B. LÓPEZ MIRANDA, F. MEDINA, D. MEDINA-ROQUE, M. NAVARRO, N. PANADERO, I. PASTOR, M. C. RODRÍGUEZ AND TJ-II TEAM Laboratorio Nacional de Fusión, CIEMAT, Madrid, Spain

Abstract

Plasma core fuelling is a critical issue for magnetic confinement fusion. Currently, the preferred technology is pellet injection where small cylinders of hydrogen ice are injected at high speeds into confined plasma and pellet injectors are operated now on many MCF devices, both tokamaks and stellarators. As the accelerated ice penetrates the hot plasma it is ablated by plasma particle impacts, its ablation rate, and thus penetration depth, being determined principally by plasma electron temperature and to a lesser extent by electron density. As it is being ablated, light emitted from the neutral cloud that surrounds and detaches occasionally from it provides a means to follow ablation and to determine penetration depth. Although light profiles are sensitive to plasma parameters, they may also exhibit overlying structures such as striations, associated with detaching plasmoids. In the case of the stellarator TJ-II, Balmer H α profiles are recorded for all injections. After reviewing its data-base, large reproducible transient structures are found occasionally in these H α signals. While the profiles can be well reproduced by simple models such large transient structures are not be explained by plasma parameter variations alone. Rather their occurrence can be associated with the presence of low-order rational surfaces in the core region. Moreover, such structures can disappear as the net plasma current is varied to modify the rotational transform profile. Examples of ablation profiles, with and without such structures, for pellet injections into neutral beam injection heated plasmas of TJ-II are presented and discussed here for a range of magnetic configurations.

1. INTRODUCTION

Cryogenic pellet injectors are widely employed for fuelling in magnetic fusion confinement devices, for instance, in the stellarator TJ-II [1, 2]. When a pellet is injected into hot confined plasma it is ablated continuously by plasma particle impacts, the rate being strongly dependent on local electron temperature and, to a lesser extent, on electron density. Pellet penetration can be determined by following the resulting Balmer H α emissions from neutral clouds that surround, and detach periodically from, the pellet. Such detachments can give rise to oscillations, often called striations, in H α signals [3, 4]. Fast-particle populations can also affect ablation, for instance, fast electrons may cause pellet destruction [5]. Here, we report on significant structures observed in H α emission profiles for injections into different TJ-II magnetic configurations that cannot be readily related to thermal electron profiles or to fast-electron or fast-ion populations. Rather, it is found that, for particular magnetic configurations, the presence or absence of structures is dependent on the net plasma current. It is postulated that the occurrence of such structures is correlated to the radial location of low-order rational surfaces.

2. EXPERIMENTAL ARRANGEMENT

TJ-II is a 4-period mid-sized heliac-type stellarator with major radius of 1.5 m, average minor radius, a, ≤ 0.22 m, a plasma volume contained within the last-closed flux-surface (LCFS), V_{plasma} , of ≤ 1.1 m³, and on-axis magnetic field, B_0 , that is ≤ 1.1 T [6]. It is designed to explore a broad range of rotational transforms, $(0.9 \leq \iota_0/2\pi \leq 2.2)$, in low, negative shear configurations ($\Delta \iota/\iota < 6\%$). Here, ι_0 is central iota and $\iota/2\pi = n/m$, where n and m are toroidal and poloidal helical winding numbers, respectively. Plasmas are initiated using microwave power provided by 2 gyrotrons operating at 53.2 GHz ($P_{\text{ECRH}} \leq 500 \text{ kW}$). Next, two tangential Neutral Beam Injector (NBI) systems, which are operated in a co-/counter- configuration (parallel/anti-parallel to the direction of the toroidal magnetic field), provide up to ~ 1 MW of through-port power at ≤ 32 keV for ≤ 120 ms [7]. With this NBI power, n_{e0} , T_{e0} , and T_{i0} up to 9×10^{19} m⁻³, 450 eV, and 130 eV, respectively, are achieved, but not simultaneously, when boron plus lithium coatings are applied to the inner vessel wall [8]. It is equipped also with a wide range of diagnostics [9].

2.1 Pellet Injector on TJ-II

A pipe-gun type pellet injector system is used on TJ-II [10]. Within its 4 formation pipes, cylindrical pellets with diameters of 0.5 mm, 0.66 mm, 0.76 mm, and/or 1 mm can be made (pellet lengths are similar to diameters). Straight guide pipes direct them to the plasma outer edge. These pipes are separated both vertically and horizontally by 25.4 mm and are arranged so that flight paths of pellets exiting 2 of the tubes pass through the magnetic axis (upper path in Fig. 1) whereas the flight paths for pellets exiting the other two have nearest approach at $\rho = \sim 0.2$ to ~ 0.4 (lower path in Fig. 1), depending on magnetic configuration. Here, $\rho = r/a$ is normalized plasma

radius where r is radius. As H_2 gas at high pressure is used to accelerate pellets to velocities between 800 m s⁻¹ and 1200 m s⁻¹, jump gaps and vacuum expansion volumes minimize gas pressure build-up in the tubes and the gas that reaches the main vacuum chamber. In all cases, pellet velocities and masses are determined using in-line light-gate and microwave cavity diagnostics. As separations between the latter and the LCFS in vacuum are known for magnetic configurations, it is possible to plot Balmer Hα emission, from analysis of light transmitted through a narrowband interference filter (660 +/- 2 nm) and an optical fibre set on the airside of a viewport in the same machine sector, versus distance into plasma. This light impinges on a silicon diode detector which produces an output voltage. When relating Hα signal to pellet radial position, corrections for toroidal/poloidal deflections due to unbalanced NBI heating are taken to be minimal [11].

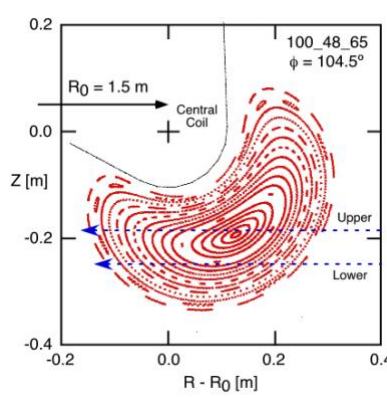


FIG. 1: Poincaré plot of field lines at TJ-II toroidal angle 104.5° , where pellet injection is performed, for the 100_48_65 magnetic configuration. Expected flight paths for pellets exiting the upper and lower guide tubes are highlighted by dash-dash arrows. R_0 is major axis, Z is vertical position below/above the central coil axis.

2.2 Balmer $H\alpha$ emissions during pellet ablation

A scaling law is used to predict pellet ablation and penetration depth in TJ-II. It considers strong neutral gas shielding and assumes no potential drop at the neutral cloud/background plasma boundary [12]. Here, strong signifies that cloud shielding dominates, so the ratio of heat flux passing through the cloud and reaching the ice surface to primary heat flux in the surrounding plasma is <<1. For H_2 pellet ablation in NBI-heated plasma it is

$$N [H/s] = 1.94 \times 10^{14} \cdot n_e^{0.45} \cdot T_e^{1.72} \cdot r_p^{1.44} \cdot \epsilon^{-0.16} \cdot A_p^{-0.28} \cdot Z_p^{-0.56} \cdot (\gamma - 1)^{0.28}$$
 (1),

where n_e and T_e are 1 electron density [cm⁻³] and temperature [eV], respectively, r_p is pellet radius [cm], ϵ is sublimation energy [eV], A_p is atomic mass, Z_p is nuclear charge number and γ is gas adiabatic index [13]. For hydrogen, $\epsilon = 0.0053$ eV, $A_p = 1$, $Z_p = 1$, and $\gamma = 7/5$.

2.3 Magnetic configurations

Magnetic configurations are created in TJ-II using several sets of external field coils. For instance, its toroidal field is created by 32 coils, called toroidal field coils, whereas the 3-dimensional twist of the central axis is created using a single set of coils: 1 circular plus 1 helical. Also, a set of vertical field coils control the plasma's vertical position. The resultant bean-shaped magnetic flux surfaces are defined completely by the combined action of preprogrammed currents in these external coils (vacuum magnetic configuration). For identification purposes, labels consist of 3 numbers, xxx yy zz, these being proportional to the central, helical and vertical currents, respectively.

2.4 Rotation transforms and iota profiles

Error sources affecting magnetic fields in TJ-II are discussed in [14], an important point being that modifications to flux surface geometry due to finite plasma pressure are minimal whereas modifications to the rotational transform profile can be significant when net plasma current is not zero. One possible source of plasma current is runaway electrons, with energies up to 1.5 MeV, generated during magnetic field ramp-up. However, prior to plasma start-up, these are blocked by a fast-reciprocating paddle. Other sources include bootstrap- and ECRH-induced currents. Although it is operated without active current compensation, net currents are typically < 1 kA during the ECRH phase. However, larger currents can be achieved by predetermined adjustment of the ECRH beam injection angle [15]. TJ-II is equipped also with 2 tangential NBI heating beams operated in a co-/counter

configuration to minimize beam driven currents. However, if unbalanced NBI heating is used, the resulting beam driven current may be enough to modify the rotational transform profile. This is discussed elsewhere [16]. It is noted that beam driven currents arise from 2 contributions: fast-ion current and a plasma electron response that shields that current. Thus, when plasma is present, the rotational transform profile, $\iota(\rho)/2\pi$, can be modified by the resulting net plasma current, I_p , as outlined in [17]. At present, there is no proven method to determine the rotational transform experimentally with any degree of accuracy in TJ-II. However, an estimate of the plasma-current radial distribution is obtained by assuming Spitzer resistivity [18]. Hence, based on that assumption, a simplified model is formulated for estimating this profile in the presence of net plasma current [19]. It is

$$(\iota(\rho)/2\pi)_{plasma} = (\iota(\rho)/2\pi)_{vacuum} + C(\rho) \cdot I_p$$
 (2).

Here $C(\rho) = A \exp(-\rho/B)$, $A = 0.1107 \, kA^{-1}$ and B = 0.3557. With this, for example, the position of the 8/5 rational surface, located near $\rho = 0.33$ for 100_48_64 in vacuum, shifts to $\rho = 0.62$ if $I_p = -1$ kA but is absent from the rotational transform profile if $I_p = +1$ kA [20]. This is introduced as it is considered that radial locations of specific low-order rational surfaces may influence pellet ablation, and hence the H α light profile. This is investigated by injecting pellets into plasmas created using different magnetic configurations and net plasma currents.

3. EXPERIMENTAL RESULTS AND DISCUSSIONS

Hα emission profiles are presented here for injections into NBI-heated phases of discharges created using selected magnetic configurations. These are for 100_28_59 (a=0.171 m, $t_0/2\pi=1.375$, $V_{plasma}=0.863$ m³), 101_42_63 (a=0.191 m, $t_0/2\pi=1.534$, $V_{plasma}=1.079$ m³), 100_44_64 (a=0.1925 m, $t_0/2\pi=1.551$, $V_{plasma}=1.098$ m³), 100_46_65 (a=0.192 m, $t_0/2\pi=1.575$, $V_{plasma}=1.092$ m³), 100_48_65 (a=0.191 m, $t_0/2\pi=1.591$, $V_{plasma}=1.09$ m³) and 100_52_66 (a=0.2 m, $t_0/2\pi=1.631$, $V_{plasma}=1.184$ m³). Here $t_0/2\pi$ is on-axis rotational transform and the volume-averaged magnetic field strength, $_{vol}$, is between ~0.93 T and ~0.96 T. Next, plasma with H_2 as the working gas is created using ECRH and once developed, additional heating, provided by one or both NBIs, maintains the plasma while ECRH is switched-off. During the NBI phase, n_{e0} can reach values above $2x10^{19}$ m⁻³ while $T_{e0} = \sim400$ eV. When a pellet with between $\sim10^{19}$ and $\sim2.5x10^{19}$ H atoms is injected, its ice penetrates beyond the magnetic axis and is fully burnt out before reaching the inner plasma edge [21]. In contrast, larger pellets may not be fully burnt out before exiting the plasma.

3.1. Injections into 100_48_65

Hα emission profiles for intact injections into the NBI-heated phase (nearly balanced) of a series of reproducible discharges made with the 100_48_65 configuration are shown in Fig. 2, (435 kW of NBI#1 at 30 kV and 340 kW of NBI#2 at 27 kV), where a single pellet is injected ~38 ms after ECRH switch-off. For these, $< n_e > = 2.2 +/- 0.1 \times 10^{19}$ m⁻³, $T_{e0} = 0.42$ keV and $I_p \sim 0$ kA at injection. In Fig. 2a, the Hα signal rises above background once the ice penetrates a few centimetres inside the LCFS. This delayed rise at outermost radii is attributed to reduced ablation due to low edge n_e and T_e [12]. Then, as the ice penetrates into hotter more dense plasma, the Hα signal rises steeply until a significant, and reproducible, drop occurs. See Figs. 2a and 2b. The drop, which is transient, occurs while the ice is between ~6 cm and ~11 cm from the plasma outer edge. At maximum drop, the light signal falls by ~50% when compared with the predicted signal. Then, once the ice has traversed these radii, the light signal recovers before reducing steadily until ablation is completed. When distance from plasma edge is transposed to ρ , this transient signal drop occurs between $\rho = 0.5$ and 0.3. When Hα signals from reproducible injections/ discharges are overlayed, see Fig. 2b, the drop is well reproduced, this pointing to a plasma effect rather than a pellet one (jitter in Hα signal shape and drop is attributed to pellets exiting guide tubes with a small scattering cone and to pellet size variation, +/- 15%).

Injections are repeated into plasmas created with the same configuration but maintained with unbalanced heating. See Fig. 2c. In a first case, 480 kW of NBI#1 at 31 kV and $I_p=+0.9$ kA (co-counter NBI), the large dip in H α signal is not reproduced, rather repeating oscillatory-type structures are seen. The structures, which occur every 5 to 10 us, are considered striations attributed to periodic detachments of the neutral cloud from about the ice [3]. For comparison, an H α profile for a pellet injected into plasma maintained by unbalanced counter NBI heating, 480 kW of NBI#2, 29 kV and $I_p=-0.95$ kA, is shown in Fig. 2d. Its profile is similar to the profiles in Figs. 2a and 2b, except that the large dip is shifted slightly outwards. Note; the small peak after the ice crosses the magnetic axis at 0.25 m into the plasma is attributed to a localized fast-electron population [6].

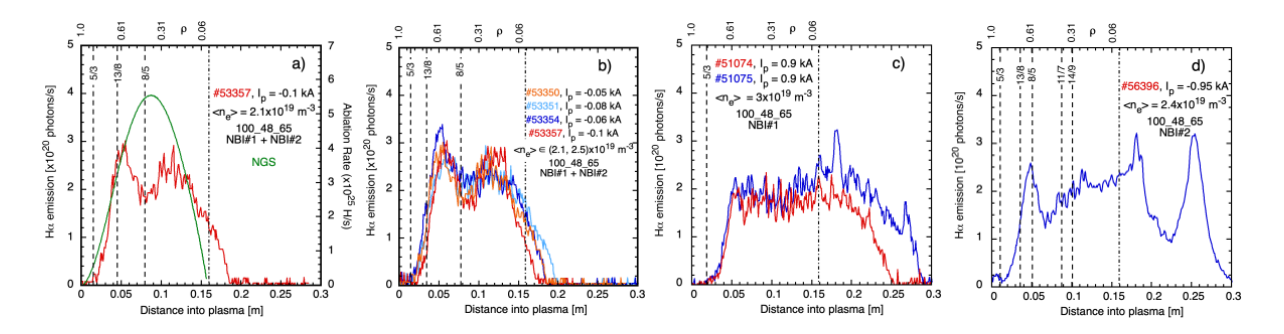


FIG. 2: Balmer H α emissions for pellet injections into selected plasmas created in TJ-II using the 100_48_65 configuration with balanced (both NBIs) or unbalanced (single NBI) heating. Traces are plotted as a function of distance into plasma from its outer edge. Vertical dash-dash lines indicate predicted locations of low-order rational surfaces for plasma current, I_p , measured just prior to each injection. <ne> is target line-averaged density. Plots are a) a pellet injected into a discharge with I_p = -0.1 kA (predicted ablation rate is shown in green), b) pellets injected into reproducible discharges of the same series as a), c) 2 pellets injected into discharges with I_p = -0.9 kA and d) a pellet injected into a discharge with I_p = -0.95 kA. A vertical dash-dot line indicates when a pellet has it nearest approach to the magnetic axis. Normalized radii are shown above plots.

3.2 Injections into 100_44_64

Hα profiles for intact pellet injections into discharges made with the 100_44_64 configuration are shown in Fig. 3. Here, pellets are injected into both balanced and unbalanced NBI-heated plasmas using the same line-of-flight as in sub-section 3.1. In Fig. 3a, injections are made into discharges heated by the counter NBI only, 400 kW of NBI#2 at 30 kV with $I_p \in (-0.7 \text{ kA}, -0.45 \text{ kA})$. Again, Hα rises above background once a pellet penetrates a few centimetres inside the LCFS, this delay being due to reduced T_e in the edge region. Next, as a pellet penetrates into hotter plasma, Hα rises until a reproducible dip occurs, *i.e.*, once the ice has travelled ~8 cm into the plasma. Then, after traversing several centimetres, Hα rises again until the pellet reaches the magnetic axis, after which the signal level drops again. Next, in Fig. 3b, pellets are injected into discharges maintained with nearly-balanced NBI heating conditions similar to those employed in Figs. 2a & 2b (435 kW of NBI#1 at 30 kV and 340 kW of NBI#2 at 27 kV). In these, with $I_p \in (-0.09 \text{ kA}, 0.01 \text{ kA})$, some structuring is seen in the Hα profiles between ~4 and ~6 cm inside the plasma. Following that, Hα signals contain random oscillations, except close to 8 cm from the plasma edge where a reoccurring dip is observed. Next, in Fig. 3c, injections are performed into discharges from the same series as in Fig. 3a but maintained using co-counter NBI heating (390 kW of NBI#1 at 30 kV) with $I_p \in (0.34 \text{ kA}, 0.5 \text{ kA})$. In these examples, Hα signals rise steadily with small non-reproducible oscillations until

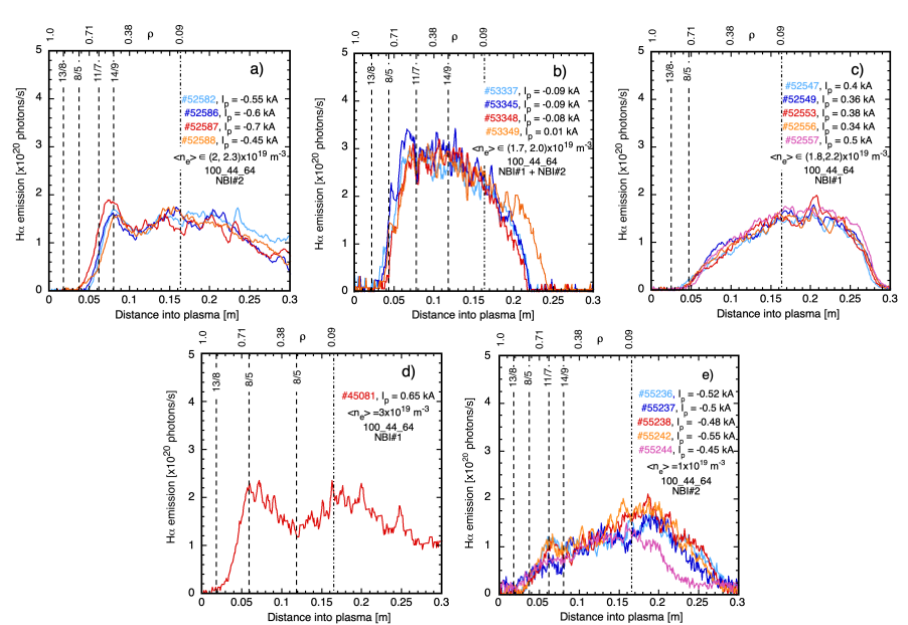


FIG 3: Balmer H α profiles for intact pellets injected into discharges created using the 100_44_64 magnetic configuration and heated by different NBI set-ups. These are a) NBI#2, b) NBI#1 plus NBI#2, c) and d) NBI#1 only, and e) NBI#2 only with reversed toroidal B field. Plasma current, I_p, just prior to injection and locations of selected low-order rational surfaces (vertical dash-dash lines) predicted using eq. 2 are indicated. <n_e> is target line-averaged density. A vertical dash-dot line indicates the distance into plasma when a pellet has nearest approach to the magnetic axis. Normalized radii are shown.

the ice has crossed the magnetic axis. Another injection, into discharge #45081 maintained using co-counter NBI heating (515 kW of NBI#1 at 30 kV) but with slightly higher plasma current, $I_p = 0.65$ kA, is shown in Fig. 3d. As in other cases, H α rises steadily initially but then begins to reduce beyond ~6 cm from the plasma edge. It continues to fall steadily until ~12 cm when the signal starts to rise again until its penetrates the axis. Again, small oscillations are superimposed this structure. Finally, single pellets are injected into a series of unbalanced NBI-heated plasmas (410 kW of NBI#2 at 29 kV or 450 kW of NBI#2 at 30 kV) with $I_p \in (-0.45 \text{ kA}, -0.55 \text{ kA})$ made with the B-field reversed, *i.e.*, B follows a clockwise direction (see Fig. 1 of [22]), thus NBI#2 is operated in co-counter configuration (parallel to the toroidal magnetic field direction). In Fig. 3e, H α profiles for such injections reproduce, to a large extent, the H α profiles shown in Fig. 3c when co-counter NBI heating (390 kW of NBI#1 at 30 kV) with $I_p \in (0.34 \text{ kA}, 0.5 \text{ kA})$ was used for the nominal B-field direction (counter clockwise from above).

3.3 Injections into other magnetic configurations

In the TJ-II pellet database, the majority of injections into NBI-heated plasma have been into discharges made using the 100 44 64 configuration. Nonetheless, there exist examples of injections made into the NBI-heated phase of discharges created using other magnetic configurations, some of which are highlighted here. For instance, in Figs. 4a and 4b, ice pellets are injected into discharge #39581 created using the 100_28_59 configuration when heated initially using unbalanced counter heating (400 kW of NBI#2 at 29 kV, I_p = -2.8 kA) and later when sustained with co-counter heating (500 kW of NBI#1 at 33 kV, $I_p = 0.35$ kA). In the first instance, the rise of H α signal is delayed until the ice has penetrated 7 cm into the plasma, at which point there is a sharp growth in Hα followed by a significant fall in signal level when at 9 cm. This is followed by slow signal oscillations until ablation is complete. In the second instance, $H\alpha$ shows a rapid rise and fall in signal level when the ice is between 3 and 6 cm into the plasma followed by oscillations about a constant level until ice burn out. Next in Figs. 4c and 4d, pellets are injected into discharges created using the 101 42 64 configuration. In the case of Fig. 4c, nearly balanced NBI heating is employed (460 kW of NBI#1 at 31 kV and 470 kW of NBI#2 at 31 kV) with $I_p \in (-0.2)$ kA, 0.11 kA) whilst in Fig. 4d, co-counter NBI heating is employed (505 kW of NBI#1 at 30 kV) with $I_p \in (0.85$ kA, 1 kA). For both these heating set-ups, no significant structures are observed in the Hα signals, rather show small oscillations while rising to their maxima and decaying slowing thereafter. Next, in Fig. 4e, pellets are injected into discharges #51066 and #51068 created with the 100 46 65 configuration using co-counter NBI heating only (480 kW of NBI#1 at 31 kV) with I_p ∈ (1 kA, 1.25 kA). Again, no significant structures are observed

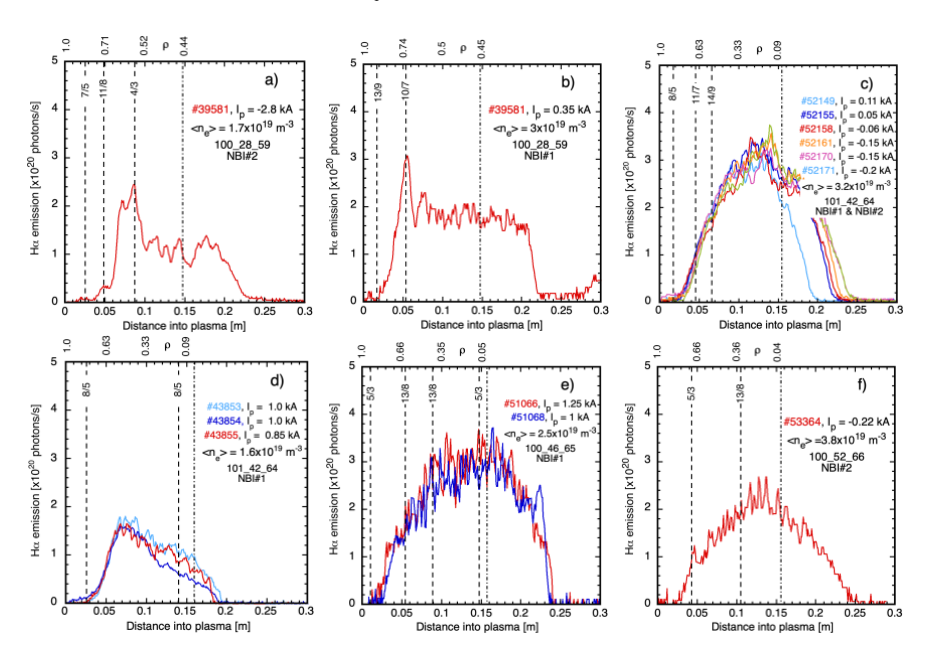


FIG. 4: Balmer $H\alpha$ profiles for pellets injected into plasmas, created by different magnetic configurations, with balanced (both NBIs) or unbalanced (single NBI) heating, or ECRH. Traces are plotted as a function of distance into plasma from its outer edge. Plots are for injections into 100_28_59 discharges with a) NBI#2 only and $I_p = -2.8$ kA, and b) NBI#1 only and $I_p = 0.35$ kA, into 101_42_64 discharges c) with nearly-balanced NBI heating and $I_p \in (-0.2$ kA, 0.11 kA) and d) with NBI#1 only and $I_p \in (0.8$ kA, 1 kA), into e) 100_46_65 discharges with NBI#1 only and $I_p \in (1$ kA, 1.25 kA), into a f) 100_52_66 discharge with NBI#2 only and $I_p = -0.22$ kA. Normalized radii are shown above plots. Vertical dash-dot lines indicate distances into plasmas when a pellet has nearest approach to the magnetic axis. $< n_e >$ is target line-averaged density. Vertical dash-dash lines are predicted locations of low-order rational surfaces.

in the H α profiles, rather, oscillations are present. Finally, in Fig. 4f, a pellet is injected into discharge #53364 created using the 100_52_66 magnetic configuration. For this, both NBI systems are employed (435 kW of NBI#1 at 30 kV, 340 kW of NBI#2 at 27 kV, and I_p = -0.22 kA) and no large structures are seen in the H α profile which is dominated by oscillations.

In Figs. 2, 3 and 4, the predicted radial locations of low-order rational surfaces for I_p 's measured just prior to ice injection are identified by vertical dash-dash lines, these locations being determined using eq. 2. Rotational transforms are plotted for magnetic configurations 101_28_59 , 101_42_63 , 100_44_64 , 100_46_65 , 100_48_65 and 100_52_66 for vacuum and for selected I_p values in Figs. 5a through to 5f, respectively. Finally, in Figs. 5g and 5h, the radial locations of selected low-order rational surfaces are shown as functions of I_p for the same configurations. Possible correlations between those surfaces and large structures in $H\alpha$ emission profiles are discussed in the following section.

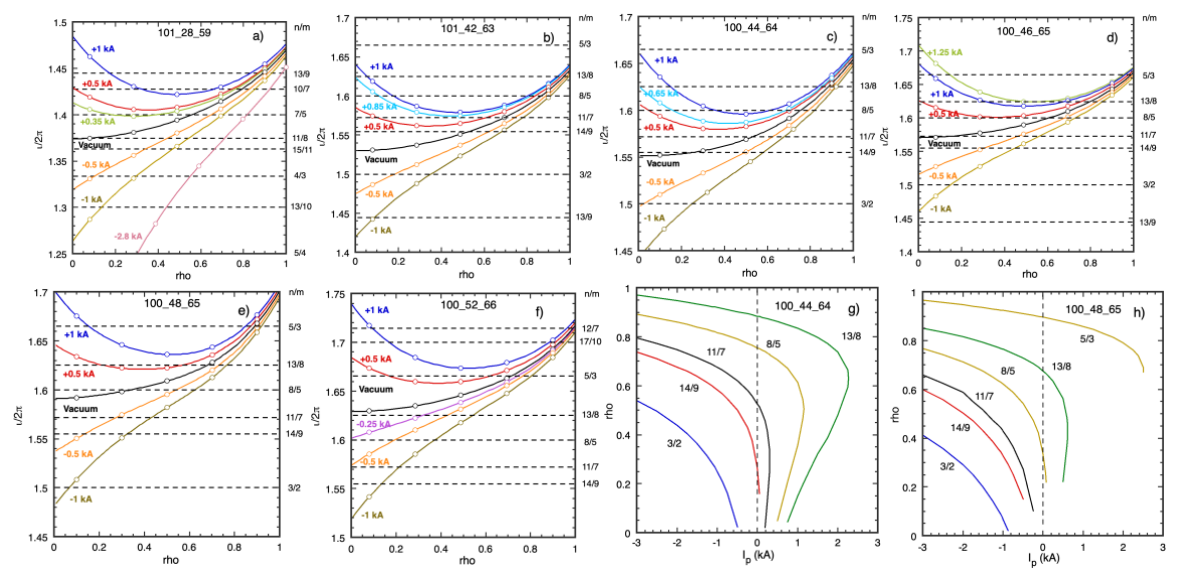


FIG. 5. Rotational transform profiles of magnetic configurations a) 101_28_59 , b) 101_42_63 , c) 100_44_64 , d) 100_64_65 , e) 100_48_65 and f) 100_52_66 for vacuum and for selected I_p values. Low-order rationals with $n \le 20$, $\nu/2\pi = n/m$, are highlighted by horizontal dash-dash lines. Next, radial locations of selected low-order rational surfaces as a function of I_p for g) 100_44_64 and h) 100_48_65 , as determined using eq. 2. Profiles are plotted for the nominal toroidal B field direction. In the case of a reversed B field, I_p 's are reversed.

4. ANALYSIS AND DISCUSSION

In many instances Balmer Hα emission profiles for pellet injections into TJ-II plasmas can be considered to be consistent with ablation rates based on target temperature and density profiles [12, 22]. Indeed, when the stellarator version of the pellet ablation code HPI2 is used to model ablation in TJ-II, good agreement can be achieved between experiments and predictions, in particular for the ECRH phase [11, 12]. In the case of ECRH plasma, pellets do not penetrate beyond the magnetic axis due to high electron temperatures, < 1.5 keV, and profiles peak before reaching the magnetic axis. In the case of well-developed NBI-heated plasma, pellets penetrate well beyond the axis due to lower electron temperatures. In both scenarios, oscillations due to striations are observed frequently in profiles, their duration being longer in NBI plasmas. However, as shown here, profiles with significant abrupt changes in Ha intensity are often observed but not well reproduced by the model of eq. 1 or by HPI2. In Figs. 2, 3 and 4, such structures are observed for both balanced- and unbalanced-NBI plasmas as well as for different magnetic configurations and plasma target densities. In order to understand the source(s) of such structures several plausible causes can be examined. For instance, it is known that pellets do not always travel along straight paths through the confined plasma, rather deflections can occur because of asymmetric particle impacts that cause, for instance, a rocket effect [23, 24, 25]. Similarly, if unbalanced NBI heating is applied, then non-uniform ablation of the pellet can accelerate it in the direction of the force imbalance and, as a result, reduce pellet penetration depth. Indeed, toroidal deflections are observed when unbalanced NBI-heating is employed in TJ-II, these being associated with momentum transfer from NBI fast ions or to a combination of these and heating asymmetries. However, such effects do not give rise to significant structures in Hα profiles. See for instance, Fig. 9 of ref. [11]. It should be noted that NBI neutral atoms cannot reach the sector into which pellets are injected, thus direct neutral beam/pellet interactions do not occur in TJ-II while, in the case of fast ions, studies indicate that their population grows towards the plasma centre whereas observed structures tend to occur $\rho = 0.75$ and 0.4 [16]. Next, fast

electrons, generated during the ECRH phase of TJ-II, can remain during the initial low-density phase of NBI-heated plasmas. However, such populations, which occur close to the magnetic axis, tend to destroy pellets as they possess velocities that are sufficient for penetrating the shielding cloud before depositing their energy in the ice [6]. Another plausible explanation might be $H\alpha$ emissions from detached outward/downward drifting plasmoids [11, 26]. However, such contributions are negligible when compared to $H\alpha$ emissions from direct particle impacts on shielding clouds during the initial stage of ablation and only become detectable once a pellet has penetrated deep into the TJ-II plasma [26]. Finally, pellet tumbling during flight or pellets passing through the centre of a rotating island would cause the magnitude of signals to vary considerably from injection to injection [3], thus structures due to such effects would be irreproducible. Thus, an alternative explanation is explored below.

From Hα plots shown here, it is found that large transient structures are absent for injections made into discharges in which low-order rational flux surfaces are predicted, by eq. 2, to be absent in the region inside $\rho = 0.8$. See Figs. 2c, 3c, 3e, 4d, 4e, 4f and 5. In contrast, significant structures appear near positions where the 8/5 rational surface is predicted to be. See Figs. 2b, 2d, 3d and 5. Similarly, structures occur near radii where other low-order rational surfaces are predicted to be, e.g., near 14/9 in Fig. 3a, near 4/3 in Fig. 4a and near 10/7 in Fig. 4b. Finally, small narrow reproducible structures occur close to the 8/5 and 11/7 rational surfaces in Fig. 3b. Now, regarding Fig 5e, 100_48_65 with $\iota_0/2\pi_{vacuum}=1.591$, it is apparent that, when I_p increases from 0 kA to +0.9 kA, the radial region $\rho = 0.2$ to 0.8 become clear of low-order rational surfaces, i.e., 8/5 and 13/8 are expelled, thus the H α signal in Fig. 2c exhibits superimposed oscillations only. In contrast, if I_p is -0.9 kA, as seen in Fig. 5e, the 8/5 surface is pushed radially outwards and when a pellet is injected, a structure is observed just inside its predicted radial location. Similar observations are seen for the 100_44_64 configuration ($\iota_0/2\pi_{\rm vacuum} = 1.551$) as I_p varies. This is particularly notable for Fig. 3c (nominal toroidal B direction) and Fig. 3e (reversed toroidal B direction) where $I_p \in (0.34 \text{ kA}, 0.5 \text{ kA})$ and $I_p \in (-0.45 \text{ kA}, -0.55 \text{ kA})$, respectively. In this situation, the locations of loworder rational surfaces should coincide for both cases and similar profiles should be observed, as is the case. Thus, this provides good evidence that, in TJ-II, ablation profiles are influenced by the presence of low-order rational surfaces inside $\rho = 0.8$. Given that the number of toroidal turns of a field line needed to cover a flux surface increases exponentially near low-order rational surfaces, it is not unexpected that a pellet's ablation rate should drop in the vicinity of such surfaces. Nonetheless, such a hypothesis requires further investigation. For instance, the iota profiles presented in Figs. 5 are based on eq. 2 as it is not possible to determine them using, for instance, the Motional Stark Effect diagnostic [27], thus there may be significant uncertainty. However, recent work simulating the temporal evolution of rotation transforms from estimates of the different current sources and the radial diffusion of shielding current might help reduce such uncertainties and thus aid in these interpretations [28].

5. CONCLUSIONS

H α light ablation profiles with unexplained structures that were obtained during pellet injections into the ECRH or NBI-phase of TJ-II plasmas are presented and discussed here. Such structures cannot be related directly to structures in target electron temperature or density profiles nor to striations, pellet deflections, fast ions or fast electron populations. From analysis of the H α profiles presented here for a range of magnetic configurations and plasma heating set-ups, it is considered that their presence or absence is related to the radial locations of low-order rational surfaces and the dependence of these locations on plasma currents. It is found that structures are not seen in profiles when certain low-order rational surfaces are absent inside $\rho = \sim 0.8$ (H $_{\alpha}$ light is not detected outside of this radius). Moreover, when such surfaces are present, the structures appear to occur close to, or just inside, such radial locations. Given that the number of toroidal turns of a field line needed to cover a flux surface increases exponentially near low-order rational surfaces, it can be argued that a pellet's ablation rate should drop in the vicinity of such surfaces. The observations reported here from the TJ-II support such an argument, at least qualitatively. Whilst additional dedicated experiments can support this argument, the reproduction of profiles using ablation simulations which consider such contributions would strengthen it considerably.

ACKNOWLEDGEMENTS

This work has been carried out within the framework of the EUROfusion Consortium, funded by the European Union via the Euratom Research and Training Programme (Grant Agreement No 101052200 - EUROfusion). Views and opinions expressed are however those of the author(s) only and do not necessarily reflect those of the European Union or the European Commission. Neither the European Union nor the European Commission can be held responsible for them. This work is partially financed by grants PID2020-116599RB-I00 and PID2023-148697OB-I00 funded by MCIN/AEI/10.13039/501100011033 and by ERDF A way of Making Europe.

REFERENCES

- [1] COMBS, S. K., and BAYLOR, L. R., Pellet-injector technology Brief history and key developments in the last 25 years, Fusion Sci. Tech. 73 (2018) 493.
- [2] PÉGOURIÉ, B., Review: Pellet injection experiments and modelling, Plasma Phys. Control. Fusion 49 (2007) R87.
- [3] PÉGOURIÉ, B., DUBOIS, M. A., Magnetic surfaces and striations during pellet ablation, Nucl. Fusion 29 (1989) 745.
- [4] PARKS, P. B., Theory of pellet cloud oscillations striations, Plasma Phys. Control. Fusion 38 (1996) 571.
- [5] McCARTHY, K. J., PANADERO, N., COMBS, S. K., TAMURA, N., et al., The impact of fast electrons on pellet injection in the stellarator TJ-II, Plasma Phys. Control. Fusion 61 (2019) 014013.
- [6] ALONSO, J. A., ALEGRE, D., ALONSO, J., ANTÓN, R., ARIAS-CAMISÓN, A., et al., Density profiles in stellarators: an overview of particle transport, fueling and profile shaping studies at TJ-II, Nucl. Fusion 64 (2024) 112018.
- [7] LINIERS, M., WOLFERS, G., SEBASTIÁN, J. A., ROJO, B., MARTÍN, F., CARRASCO, R., et al., Beamline duct monitoring of the TJ-II neutral beam injectors, Fusion Eng. Design 88 (2013) 960.
- [8] TABARÉS, F. L., OCHANDO, M., TAFALLA, D., MEDINA, F., McCARTHY, K., et al., Energy and particle balance studies under full boron and lithium-coated walls in TJ-II, Contrib. Plasma Phys. 50 (2010) 610.
- [9] McCARTHY, K. J., Plasma diagnostic systems and methods used on the stellarator TJ-II, J. Instrum. 16 (2021) C12026.
- [10] COMBS, S. K., FOUST, C. R., McGILL, J. M., CAUGHMAN, J. B. O., McCARTHY, K. J., et al., Results from laboratory testing of a new four-barrel pellet injector for the TJ-II stellarator, Fusion Sci. Tech. 64 (2013) 513.
- [11] PANADERO, N., McCARTHY, K. J., KOECHL, F., BALDZUHN, J., VELASCO, J. L., et al., Experimental studies and simulations of hydrogen pellet ablation in the stellarator TJ-II, Nucl. Fusion 58 (2018) 026025.
- [12] McCARTHY, K. J., TAMURA, N., COMBS, S. K., PANADERO, N., et al, Comparison of cryogenic (hydrogen) and TESPEL (polystyrene) pellet particle deposition in a magnetically confined plasma, EPL 120 (2017) 25001.
- [13] SERGEEV, V. Yu., BAHHAREVA, O. A., KUTEEV, B. V., and TENDLER, M. V., Studies of the impurity pellet ablation in the high-temperature plasma of magnetic confinement devices, Plasma Phys. Rep. 32 (2006) 363.
- [14] van MILLIGEN, B. Ph., ESTRADA, T., ASCASÍBAR, E., TAFALLA, D., LÓPEZ-BRUNA, D., et al., Integrated data analysis at TJ-II: the density profile, Rev. Sci. Instrum. 82 (2011) 073503.
- [15] TRIBALDOS, V., JIMÉNEZ, J. A., GUASP, J. and van MILLIGEN, B. Ph., Electron cyclotron heating and current drive in the TJ-II stellarator, Plasma Phys. Control. Fusion 40 (1998) 2113.
- [16] MULAS, S., CAPPA, A., MARTÍNEZ-FERNÁNDEZ, J., LÓPEZ-BRUNA, D., VELASCO, J. L., et al., Validating neutral-beam current drive simulations in the TJ-II stellarator, Nucl. Fusion 63 (2023) 066026.
- [17] van MILLIGEN, B. Ph., ESTRADA, T., CARRERAS, B., GARCÍA, L. and TJ-II team, Importance of the rotational transforms for L-H transitions in the TJ-II stellarator, Plasma 7 (2024) 446.
- [18] CASTEJÓN, F., LÓPEZ-BRUNA, D., ESTRADA, T., ASCASÍBAR, E., ZURRO, B., and BACIERO, A., Influence of low-order rational surfaces on heat transport in TJ-II heliac ECRH plasmas, Nucl. Fusion 44 (2004) 593.
- [19] MELNIKOV, A., OCHANDO, M. A., ASCASÍBAR, E., CASTEJÓN, F., CAPPA, A., ELISEEV, L., et al., Effect of magnetic configuration on frequency of NBI-driven Alfvén modes in TJ-II, Nucl. Fusion 54 (2014) 123002.
- [20] van MILLIGEN B. Ph, GARCÍA-CORTÉS, I., McCARTHY, K. J., ESTRADA, T., CAPPA, A., PONS-VILLALONGA, P., et al., The rotational transform and enhanced confinement in the TJ-II stellarator, J. Plasma Phys. 90 (2025) E98.
- [21] McCARTHY, K. J., PANADERO, N., VELASCO, J. L., COMBS, S.K., CAUGHMAN, J. B. O., et al., Plasma fuelling with cryogenic pellets in the stellarator TJ-II, Nucl Fusion 57 (2017) 056039.
- [22] McCARTHY, K. J., GARCÍA-CORTÉS, I., ALONSO, J. A., ARIAS-CAMISÓN, A., ASCASÍBAR, E., et al., Multipellet injection into the NBI-heated phase of TJ-II plasmas, Nucl. Fusion 64 (2024) 066019.
- [23] MÜLLER, H. W., BÜCHL, K., KAUFMANN, M., LANG, P. T., et al., High-β plasmoid drift during pellet injection into tokamaks, Phys. Rev. Lett. 83 (1999) 2199.
- [24] GUTH, N. J., VALHAGGEN, O., HELANDER, P., PUSZTAI, I., et al., Pellet rocket effect in magnetic confinement fusion plasmas, Phys. Rev. Lett. 134 (2025) 035101.
- [25] KOCSIS, G., TAMURA, N., BUSSIAHN, R., McCARTHY, K. J., et al., Investigation of TESPEL cloud dynamics in Wendelstein stellarator, Nucl. Fusion, 61 (2021) 016006.
- [26] PANADERO, N., McCARTHY, K. J., PÉGOURIÉ, B., CARRASCO, R., GARCÍA-CORTÉS, I, GARCÍA, et al., Using rational surfaces to improve pellet fuelling efficiency in stellarators, J. Plasma Phys. 89 (2023) 955890601.
- [27] McCARTHY, K. J., PANADERO, N., LÓPEZ-FRAGUAS, A., et al., A spectrally resolved Motional Stark Effect diagnostic for the TJ-II stellarator, Contrib. Plasma Phys. 55 (2015) 459.
- [28] PONS-VILLALONGA, P., CAPPA, Á., ASCASÍBAR, E., et al., Characterization of NBI-driven shear Alfvén waves in the TJ-II stellarator using Mirnov probes and electrostatic potential fluctuation measurements, sent to Nucl. Fusion.